Applications in Energy and Combustion Science 15 (2023) 100183

Contents lists available at ScienceDirect

Applications in Energy and Combustion Science

journal homepage: www.sciencedirect.com/journal/applications-in-energy-and-combustion-science

Small angle X-ray scattering of particle growth and structure in spray flame synthesis

Mira Simmler [a,*], Simon Buchheiser [a], Ricardo Tischendorf [b], Jalal Poostforooshan [c], Alfred P. Weber [c], Hans-Joachim Schmid [b], Hermann Nirschl [a]

[a] Karlsruhe Institute of Technology, Institute of Mechanical Process Engineering and Mechanics, Karlsruhe, Germany
[b] Paderborn University, Particle Technology Group, Paderborn, Germany
[c] Clausthal University of Technology, Institute of Particle Technology, Clausthal Zellerfeld, Germany

ARTICLE INFO

Keywords:
Small angle X-ray scattering
Spray flame synthesis
In situ
Fractal dimension of mass and surface
Primary particle sizes
Particle formation

ABSTRACT

Customized metal oxide nanoparticles are on increasing demand due to their high specific surface area coupled with their material properties. Spray flame synthesis (SFS) is able to produce such particles in high quantity and purity. However, the turbulent flame including droplets is a complex system. The analysis of the product is challenging due to the broad size distribution of the aggregated primary particles. Thus, this study combines small angle X-ray scattering (SAXS) with transmission electron microscopy (TEM) in order to gain valuable information about primary particle sizes and fractal properties. Insights about the particle formation is obtained by comparing the SAXS data of titanium oxide and iron oxide particles produced with a variety of precursors in different concentrations using two burner setups. Remarkably, all presented systems show a size distribution of the primary particle with two size fractions. The differences in the sizes and consequences for the gained information about the fractal dimensions are discussed in detail. This includes the overlap of scattering information and resolution limits. All particle structures include small particles of 5–8 nm pointing to a gas-to-particle pathway. The large particle fraction ranges from 35 to 320 nm depending on precursor composition and concentration. Their formation is likely linked to hydrolysis reactions of the precursor in spray droplets. For the aggregates, the fractal dimension of mass with values 1.6–1.8 point to diffusion-limited cluster aggregation which is typical for flame-made products. The evaluation of *in situ* studies with synchrotron radiation confirms the gas-to-particle pathway.

1. Introduction

1.1. Potential of SFS and particle synthesis pathways

Spray flame synthesis (SFS) is a fast and scalable process to manufacture numerous different high purity metal oxides with tailored properties such as aggregate shape, particle size and specific surface area [1–3]. In this process, a liquid, combustible precursor composition is atomized into a self-sustaining gas flame. Due to the ignition of the spray, a flame evolves representing a reactive, turbulent multiphase flow field. Major advantages of SFS in contrast to other competitive gas phase processes is the fact that nearly every element of the periodic table can be processed due to the usage of low-cost liquid precursor systems. Furthermore, particles form within ultra-short time periods (usually within a few milliseconds) allowing the preparation of metastable materials and phase compositions. Typically, particles evolve in two different ways in SFS: the gas-to-particle pathway and the droplet-to-particle pathway. The first pathway implies that particles originate in the gas phase by precursor evaporation and disintegration in the gas phase followed by a subsequent interplay of particle building mechanisms (nucleation, agglomeration, sintering, growth). This way, aggregates and agglomerates are synthesized consisting of small primary particles. Following the droplet-to-particle pathway, the metal precursor precipitates within the liquid phase forming large-sized solid or hollow spheres [1,3–5]. If both pathways are present, the particle outcome is highly polydisperse.

1.2. SFS of titanium oxide and iron oxide

Among SFS-made particle materials, iron oxides and titanium oxides,

* Corresponding author.
E-mail address: mira.simmler@kit.edu (M. Simmler).

https://doi.org/10.1016/j.jaecs.2023.100183
Received 30 March 2023; Received in revised form 14 July 2023; Accepted 18 July 2023
Available online 20 July 2023

have drawn specific attention because of their variety of technical applications. The particles' functional properties highly depend on the particle structure (primary particle sizes, aggregate sizes, fractal dimensions, etc.). In terms of titanium oxide, rutile particles are used as pigment because of the optimal optical properties at particle sizes around 200–300 nm (*e.g.* in white paint) [6]. If used as photo-catalysts, the particles should have high specific surface areas and consist of anatase as crystal structure [7,8]. A typical application of iron oxide is particle magnetization used for hyperthermia, magnetic resonance therapy, and drug delivery. Herein, the magnetic properties are highly dependent on the primary particle size [9–12]. Several authors investigated the influence of operating conditions on the evolution of primary particle sizes and the magnetization of iron oxides [13–15].

It is known that the precursor composition critically affects the dominance of the droplet pathway. Jossen et al. [16] postulated that the precursor's relative evaporability and the specific flame enthalpy have a strong influence on the presence of droplet pathways. From physical point of view, their model described the following: If the organic solvent evaporates before the precursor evaporates/decomposes, the precursor precipitates within the droplet. Solely, the physical precipitation of the precursor was considered whereas the precursor can undergo chemical reactions within the liquid feed.

In case of titanium oxide, the precursor titanium tetraisopropoxide (TTIP) shows a hydrolysis reaction if dissolved in ethanol [17]. Experiments of single burning droplets containing this precursor combination yield large spherical particles along with fine aggregate structures [18]. This behavior points to a coexistence of the droplet-to-particle and the gas-to-particle pathway. If acetylacetone is added to TTIP, titanium diisopropoxide bis(acetylacetonate) (TDIP) forms. Similarly to TTIP, this precursor is also prone for hydrolysis [19,20].

For the production of iron oxides, it is also well-known that iron salts tend to form solid low-volatile iron-hydroxides (IHs) if they are dissolved in aqueous or alcoholic solvents [21–25]. Stodt et al. [23] tested the stability of iron (III) nonahydrate (IN), a common precursor in SFS, in ethanol (EtOH), isopropanol (iPrOH), n-propanol and n-butanol revealing a formation of an IH-precipitate at atmospheric conditions after several days. Keller et al. [24,25] showed the same reaction for IN in EtOH and n-propanol providing thermophysical equilibrium data. Tischendorf et al. [26] used this precursor composition in SFS producing both large-sized particles and small-sized particles by the droplet-to-particle and gas-to-particle pathway, respectively. An established method to suppress the droplet-to-particle pathway are acidic solvents. For instance, the addition of 2-ethylhexanoic acid (EHA) to IN-EtOH-solutions leads to esterification and carboxylation mechanisms protecting iron ions against hydrolyzation and precipitation [17,23,27–29]. Another popular precursor for the formation of iron oxides is iron pentacarbonyl (IPC) [30]. Using this precursor in a spray flame, Grimm et al. [13] produced fine primary particles of iron oxide with sizes of around 5 nm. Their results point to a clear gas-to-particle pathway. Nonetheless, recent studies of the flame chemistry of IPC show the formation of iron hydroxides in hydrolysis reactions with water [31].

1.3. Potential of SAXS for the characterization of complex particle structures

For the characterization of the complex particle structures formed by SFS, measurement techniques for the nanoscale can be applied such as Transmission Electron Microscopy (TEM), Brunauer-Emmet-Teller N_2 physisorption (BET) and small angle X-ray scattering (SAXS). These techniques reveal reliable and comprehensive information about particle characteristics but they each bear specific disadvantages. For instance, TEM, solely allows the evaluation of 2D particle projections. Individual particle structures cannot be distinguished hindering the identification of aggregate/agglomerate structures [26]. Using BET, only an average primary particle diameter can be derived from the specific surface area, assuming a perfectly monodisperse particle ensemble. Hence, the presence of large-sized particles prohibits the correct evaluation of existing small primary particle sizes. With SAXS, the identification of different particle sizes as an average diameter or a particle size distribution is possible. Overlap of scattering or resolution limits might obscure particle characteristics. Since SAXS is an integrated measurement technique, more particles are considered than any TEM evaluation ever could. The combination of SAXS with TEM analysis ensure all particle details are identified in the right proportion. The addition of a Bonse-Hart module to a SAXS setup allows for the detection of structures in the lower micron size range [32,33]. With this extension to ultra-small angles, particles of the droplet-to-particle pathway can be observed.

To gain a more comprehensive perspective on the SFS process, *in situ* measurements were conducted. This way, it is possible to follow the spatial evolution of the particle structure properties [3,26,34–36]. Gröhn et al. [34], Mohammadi et al. [35], Suleiman et al. [36], and Tischendorf et al. [26] extracted local particle samples from SFS for evaluation by utilizing hole in tube (HIAT) probes and/or thermophoretic sampling (TS) probes. However, intrusive sampling by HIAT or TS influences the reactive flow field, consequently resulting in an unknown experimental bias [37,38]. In contrast, non-intrusive optical approaches such as wide angle light scattering (WALS), phase-selective-laser-induced-breakdown spectroscopy (PS-LIBS) and SAXS are known for a neglectable experimental interference. These techniques have been applied to SFS and shown high potential for the evaluation of synthesis pathways and revealing information about particle sizes and their elemental composition. For instance, Assmann et al. [39] used WALS to monitor *in situ* the particle sizes of titanium oxide in SFS. This way, it is possible to distinguish droplets, aggregates of gas-borne particles, and particles originating from the droplet pathway. As presented by Stodt et al. [40], PS-LIBS allows the quantification of the gas phase-species and of the particle chemical composition. Studies by Jossen [41] and Simmler et al. [42] detect primary particle sizes of zirconia in the SFS process with *in situ* SAXS experiments. In both cases of zirconia, only the gas-to-particle pathway was present. SAXS investigations of the product confirm only small primary particles for a wide range of precursor concentrations [43].

1.4. Scope

The presented studies show the broad research into SFS and its products for a wide range of precursor solutions. However, the different experimental results are difficult to compare since the experimental setups and measurement techniques differ widely. Therefore, this work aims to provide detailed information about nanoparticulate aggregates of iron oxide and titanium oxide using a highly standardized burner system and SAXS as the main measurement technique. The wide range of considered precursor compositions and concentration provides an extensive overview of the observed particulate and fractal properties. The comparison of the data allows to assess the influence of droplet sizes in combination with hydrolysis reactions on the final product.

The particles were produced in four different laboratories using two different burner setups: the standardized *SpraySyn1* burner [44] and an adapted setup using electrospray [35,45]. Together, SAXS and TEM analysis of powder samples from these experiments reveal information about the primary particle size and their polydispersity as well as fractal dimensions of the particle surface and aggregate shape. *In situ* experiments of selected precursor compositions open the discussion about the dominance of synthesis pathways (droplet-to-particle *vs.* gas-to-particle). While *in situ* SAXS was performed with synchrotron radiation, TEM samples were extracted *in situ* by using a thermophoretic sampler.

The presented results demonstrate the complexity of spray flame synthesis and the potential of SAXS to characterize the particle outcome. The focus lies on the influence of different precursors and their

concentration as well as the burner setup on the structure of the final product. A central aspect of this publication is the identification of large primary particles and their origin in the particle formation process.

2. Experimental

The here used *SpraySyn1* burner (University of Duisburg-Essen, Duisburg, Germany) was developed during the priority program SPP1980 *SpraySyn* of the German Research Foundation (DFG). The schematic graphic in Fig. 1Sa in the supplement gives a basic overview of the burner. The work of Schneider et al. [44] provides details to the dimensions and concept of the burner as well as a routine allowing a cross-comparison of all SFS studies with this burner. For the experiments with the *SpraySyn1* burner, mass flow controllers by Bronkhorst (Karmen, Germany) were used. The parameters for the gas feed are 2 slm (standard liters per minute) methane and 16 slm oxygen for the pilot flame stabilized with 120 slm sheath air. The precursor solution (fed by a syringe pump at 2 mL min^{-1}) is atomized with 10 slm oxygen.

In recent studies, the atomization and ignition for *SpraySyn1* was investigated visually by shadowgraphy and highspeed-imaging revealing flame pulsations [46,47]. The cause is an aperiodic ignition of the precursor feed. This leads to temporary fluctuations of the flame activity (measured by flame luminescence). The duration of flame pulses as well as the time span between pulses are in the single-digit microsecond regime. Hence, they are not recognizable by human eyes or by SLR recordings. To eliminate influences of the pulsations on the particle structure, experiments using electrohydrodynamic atomization (EHDA, electrospray) were conducted [35,45]. The capillary of the electrospray was positioned at 20 mm above the *SpraySyn1* burner and 40 mm from its center (see Fig. 1Sb in the supplement). To allow for an optimized atomization in the electric field, the liquid feed was reduced significantly as well as the gas feed for the pilot flame. The operating parameters and resulting flame heights for both burner setups are given in the supplement Table 1S.

This study focuses on two materials, titanium oxide and iron oxide, which are in high demand due to their unique functional properties. Different precursor compositions are considered since hydrolysis reactions influence the particle properties of the final product as explained in the introduction. Pure alcohol tends to react in similar ways if used in precursor solutions for SFS. Specifically, the difference in enthalpy of

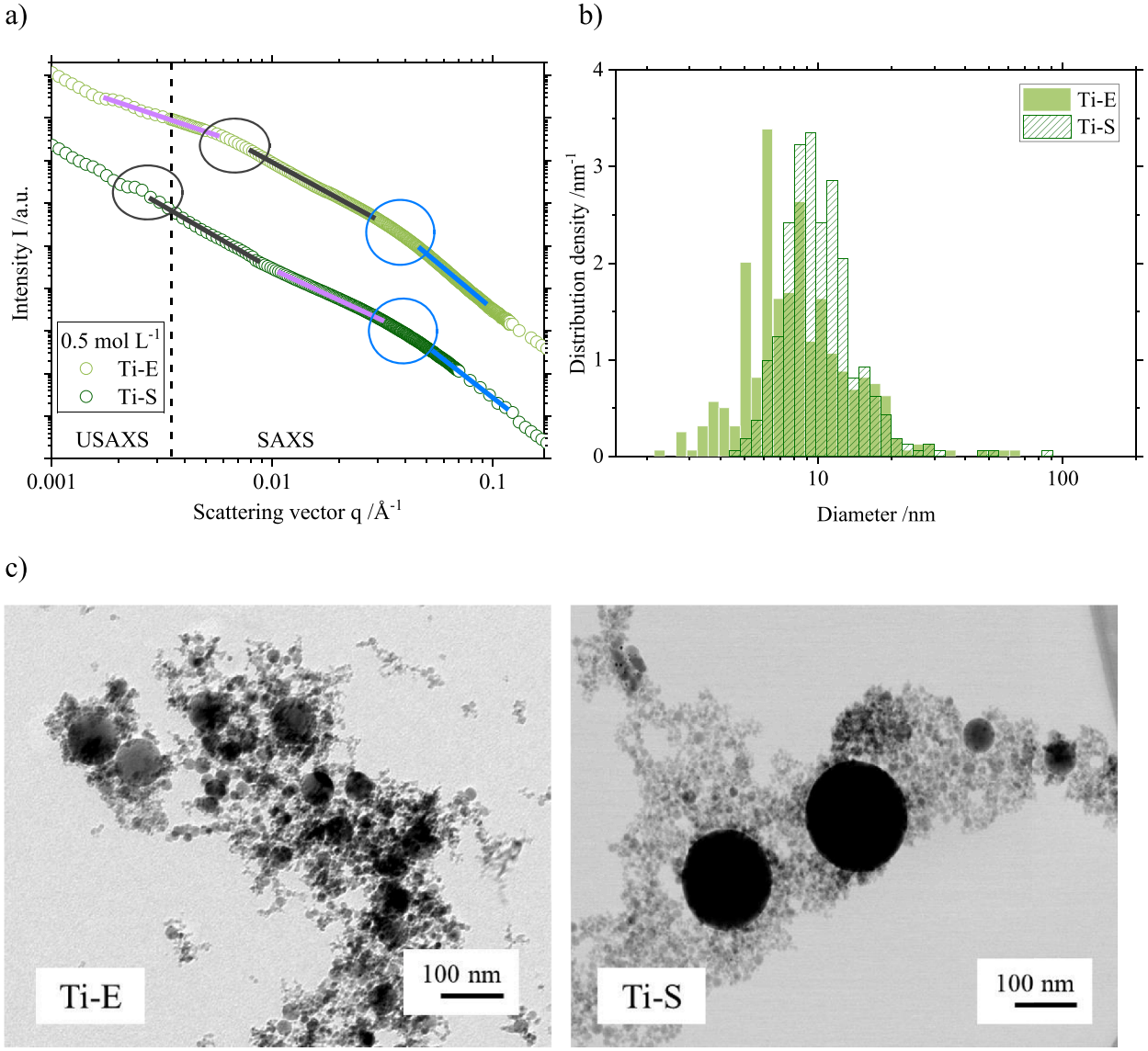

Fig. 1. Samples Ti-S and Ti-E with concentration of 0.5 mol L^{-1}. (a) (U)SAXS data including markings for the Guinier (circles) and power (lines) laws (blue = small particles, gray = large particles, purple = aggregates). (b) Number density distributions derived from TEM. (c) Exemplary TEM-images. (For interpretation of the references to color in this figure legend, the reader is referred to the web version of this article.)

Table 1
Overview of all particle samples including production details.

Sample	Product	Precursor	Solvent (v/v)	Burner	Place of experiment	Sources for setup
Ti-S	TiO_2	TTIP	100% iPrOH	S	Karlsruhe[1]	[42,43]
Ti-E	TiO_2	TDIP	100% EtOH	E	Clausthal	[35,45]
IN-S	Fe_xO_y	IN	100% EtOH	S	Karlsruhe	[43]
IN-EHA-S	Fe_xO_y	IN	35% EtOH + 65% EHA	S	Paderborn/ Karlruhe[2]	[26,42,43]
IN-E	Fe_xO_y	IN	100% iPrOH	E	Clausthal	[35,45]
IPC-S	Fe_xO_y	IPC	100% EtOH	S	Magdeburg[3]	[47]

[1] additional *in situ* experiments at the Karlsruhe Research Accelerator (KARA).
[2] additional *in situ* experiments at KARA and in Paderborn.
[3] nitrogen instead of pressured air as sheath gas
TTIP: titanium tetraisopropoxide (Thermo Fisher Scientific, Waltham, MA, USA)
TDIP: titanium diisopropoxide bis(acetylacetonat (75 wt.% in isopropanol; Sigma Aldrich, St. Louis, MO, USA)
IPC: iron pentacarbonyl (Sigma Aldrich)
IN: iron nitrate nonahydrate (Sigma Aldrich; VWR Chemicals, Radnor, PA, USA; Carl Roth GmbH, Karlsruhe, Germany)
EtOH: ethanol (VWR Chemicals; Carl Roth GmbH; Dr. Wieland GmbH, Marbach am Neckar, Germany)
EHA: 2-ethylhexanoic acid (Sigma Aldrich; Thermo Fisher Scientific)
iPrOH: isopropanol (Carl Roth GmbH; Dr. Wieland GmbH).

ethanol and isopropanol is minimal. Thus the influence on the particle size is negligible considering the polydispersity of the primary particles. For the production of titanium oxide, both burner systems are used with precursors prone for hydrolysis (TTIP and TDIP) [17,19]. This offers the opportunity to investigate the influence of hydrolysis on the particle size distribution in regard to the existence of flame fluctuations.

To gain iron oxide, the focus lies on iron nitrate in different solvents as the chemical reactions in the precursor composition effect the particle outcome. Here, both burner setups are considered as well as the use of EHA to suppress the formation of hydroxides [23]. For comparison, experiments with IPC are included since this precursor is known for the formation of only small particles via the gas-to-particle pathway [13].

Table 1 provides an overview of the used precursor compositions in the four laboratories including sources (concentration ranges, sampling method and position in the supplement Table 2S). For the *ex situ* results, the particles were extracted above the flame. The resulting powder sample was transferred on a TEM grid and polyimide foil for TEM and SAXS analysis respectively. As indicated in the footnotes 1 and 2, *in situ* experiments were conducted for both materials to investigate the particle formation. In this context, the word "*in situ*" refers to results gained by online diagnostics using X-ray radiation and extracting the particles directly in and above the flame with minimal interference using thermophoretic sampling with subsequent TEM (TS-TEM) [3].

In this work, we focus on the particle structure. However, the particle formation mechanism is dependent on the droplet size of the ignited spray. PDA measurements show the droplet evolution in the flame. In short, both burner setups generate a similar droplet size of around 25 µm at HAB = 50 mm [35,46,48]. However, the absolute value is also dependent on precursor viscosity.

For the *ex situ* results, TEM images of the particle systems were taken in Karlsruhe, Paderborn and Clausthal. One exemplary image of each particle system is displayed in the results. For each presented number density distribution, the Feret diameters of over 300 particles of multiple images were considered.

To extract particles *in situ* for TEM analysis, thermophoretic sampling (TS-TEM) was applied. A thermophoretic sampler was tailored to protect the TEM sample grid by a shielding-mechanism until reaching the sampling position. This way, an undesired sampling of particles during traversing the grid to the sampling position is avoided (shutter system) and allows adjustable sampling times from 1 to 30 ms [26].

The here presented SAXS data of the powder samples on the polyimide foil were derived with the laboratory camera Xeuss 2.0 Q-Xoom (Xenocs SA, Grenoble, France) using a Copper K-α as an X-ray energy at the Institute of Mechanical Process Engineering and Mechanics (MVM) in Karlsruhe. The sample-to-detector distance varied between 500 mm and 2500 mm with an exposure time of 10 min per measurement. The installation of a Bonse-Hart-module [32,33] yields further information at scattering vectors below 10^{-3} Å^{-1} known as U(ultra)SAXS with a measurement time of 4 h. For each powder sample, the scattering data of USAXS and measurements at different sample-to-detector distances were merged together and converted to absolute scaling using standardized glassy carbon.

The *in situ* measurements for SAXS took place at the beamline for single crystal diffractometry (SCD) at the Karlsruhe Research Accelerator (KARA) in Karlsruhe. Fig 2S in the supplement shows a picture of the setup. The wavelength was set to 0.1393 nm and the X-ray beam was shaped by a pinhole with a diameter of 1 mm. The burner was mounted to a motor with two axis and placed into the beam path. A detector with a third of the screen compared to the Xeuss 2.0 was used at a fixed distance of 1368 mm between the center of the flame and the detector with a beam stop of 4 mm in diameter. The X-ray beam penetrated the spray flame through its center at different heights above the burner (HAB). The scattering of one point in the flame and the background (50 mm to the side of the flame) were alternatingly recorded for 25 s 20 times. Summed up, this led to a measurement time of 250 s in the flame for each point [42].

SAXS data is presented as intensity I over the scattering vector q in a double logarithmic diagram with the wavelength λ of the X-ray source and the scattering angle θ between the sample and the scattering on the detector:

$$q = \frac{4\pi}{\lambda} \sin\left(\frac{\theta}{2}\right) \quad (1)$$

As the investigated particle systems are hierarchic aggregates with primary particles in different sizes, the unified fit model by Beaucage [49] was applied. The scattering data is divided into structural levels starting with the smallest particle sizes at the largest scattering vectors. Each level is assigned a power law and a Guinier fit. Detailed examples of the levels and fits can be found in Simmler at al. [43]. Due to the possible convolution of scattering information from the large primary particle fraction with the aggregates, the unified fit model was only applied to the small primary particle fraction using Irena [50] (Package 2.68, IgorPro, WaveMetrics Inc., Portland, OR, USA). Because no appropriate fitting tool for the presented particle system is available, the power law and Guinier fit for the large particle fraction were applied by hand. To identify the exponential decay of the Guiner fit, the adjoining power law fits were extended until they intersect.

The power law fit, defined by the slope p and the prefactor B, describes the fractural behavior of the particle system [51]:

$$I(q) = B\, q^{-p} \quad (2)$$

In SAXS, the fractal dimension of mass and surface can be derived.

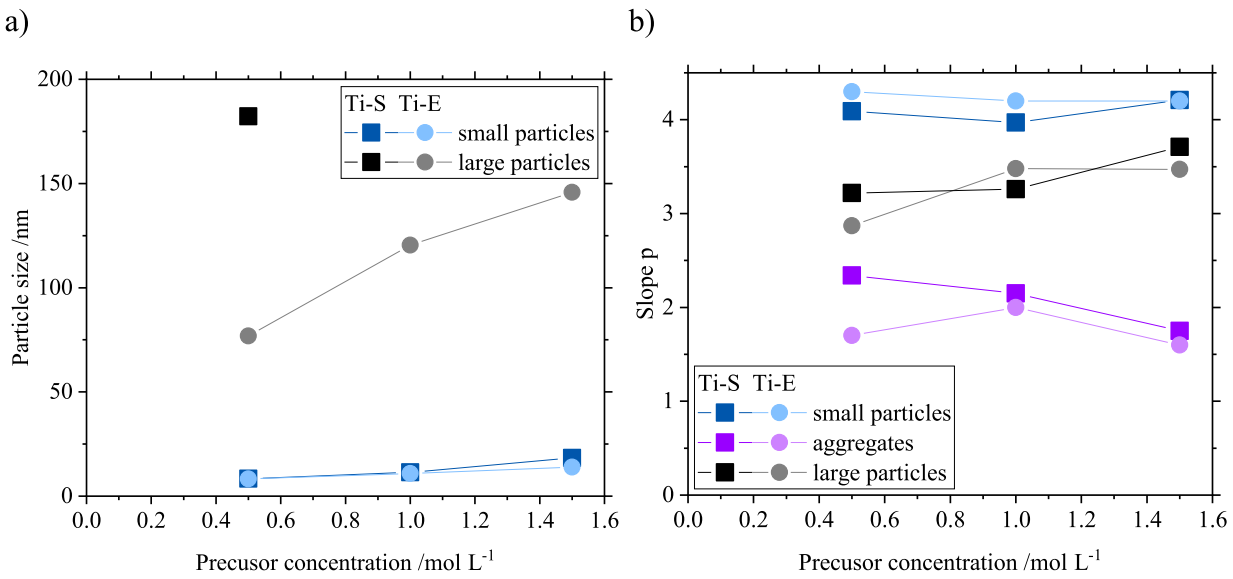

Fig. 2. SAXS results for Ti-S and Ti-E at different Ti concentrations. (a) Particle size: large particles: d_{geo} (Eq. (4)). Small particles: d_{mean} (Eq. (5)). (b) Slope p for small particles (surface fractal), aggregates (mass fractal) and large particles (surface fractal). (For interpretation of the references to color in this figure legend, the reader is referred to the web version of this article.)

Surface fractals describe the condition of the particle surfaces. The slope p can assume values between 3 and 4 [52]. If $p = 4$, the particle surfaces are smooth and have a sharp interface [53]. This is known as Porod behavior [51]. Values lower than 4 point to rough surfaces. This phenomenon was observed for carbon black [54] and zirconia particles made by SFS [43]. Additionally, cases of a slope steeper than 4 have been reported and recognized as a diffuse interface and fluctuations in density [55]. The fractal dimension of mass provides insight into the shape of aggregates. Values between 1 and 3 are physically possible for the slope p and define the dimension [52]: one describes a stringy, two a flat and three a 3-dimensional aggregate [53,56]. For flame-made structures, values of 1.7–1.8 are typical as they follow the diffusion-limited cluster aggregation [57,58].

The Guinier fit is applied at a change to a steeper slope and gives information about the particle size with the radius of gyration R_g and the prefactor G [59]:

$$I(q) = G\exp\left(-\frac{q^2 R_g^2}{3}\right) \tag{3}$$

For spherical particles, the geometric diameter d_{geo} can be derived from the radius of gyration R_g as [59,60]:

$$d_{geo} = 2\sqrt{\frac{5}{3}}R_g \tag{4}$$

If the particles are polydisperse spheres with a log-normal size distribution and $p = 4$, the mean diameter d_{mean} can be calculated with parameters of both fits [60,61]:

$$d_{mean} = 2\sqrt{\frac{5}{3}}R_g\exp\left(-\frac{13}{24}\ln\left(\frac{B\,R_g^4}{1.62\,G}\right)\right) \tag{5}$$

Eq. (5) can only be applied to the structural level of smallest particle fraction and represents a number based diameter. If the primary particles show a bimodal distribution, only the size of the small particle fraction can be determined with Eq. (5) whereas the size of larger particles should be described with Eq. (4).

3. Results and discussion

The results are divided by the product into titanium oxide and iron oxide. For both, SAXS and TEM data of each precursor composition with the concentration of 0.5 mol L^{-1} are provided. This overview of the precursor compositions is followed by more results of different precursor concentrations and *in situ* experiments.

3.1. Titanium oxide

The results of titanium oxide include the precursor compositions TTIP in isopropanol and TDIP in ethanol prepared with the *SpraySyn1* burner (Ti-S) and electrospray (Ti-E) respectively. Fig. 1a depicts the combined scattering data at (ultra-)small angles of the samples Ti-S (dark green) and Ti-E (light green). In the TEM images with the same magnification (Fig. 1c), both particle systems show aggregate structures of polydisperse primary particles with coexisting smaller and larger particles. The number density distributions derived from TEM in Fig. 1b corroborate the qualitatively observed bimodality of the primary particles. For the sample produced by the *SpraySyn1* burner (Ti-S), the distribution of the small particles is narrower in range and shifted to slightly larger diameters than the one from electrospray (Ti-E). The large particles of Ti-E do not increase as much as the ones of Ti-S.

The (U)SAXS data (Fig. 1a) confirms these observations. Generally, the region of the Guinier law fit is marked with a circle at the change to a steeper slope and the slope of the power law fit is marked with a straight line. The color code stays the same throughout this paper: blue for small particles, gray for large particles and purple for the aggregates. The data is presented in arbitrary units for better readability. However, the fit parameters were derived from the data at absolute intensity.

The Guinier fit for the smaller fraction of the primary particles (blue) at the scattering vector range of $q = 0.03$–0.05 $Å^{-1}$ yields $d_{mean} = 8.3$ nm for both samples. This value fits well with the maximum of the number density distribution derived from TEM (Fig. 1b) for the small particle fraction. The slope of Ti-S has a value of 4 (Porod behavior) corresponding to smooth particle surfaces [53]. Ti-E shows a steeper slope $p = 4.25$ which is a sign for density fluctuations and points to a diffuse interface [55]. For the large particle fraction (gray), Ti-S shows a Guinier region at the transition of USAXS to SAXS resulting in $d_{geo} = 183$ nm. As presented in Fig. 1b, the large-sized particles observed via TEM are smaller than this value. However, scattering impacts the number based particle diameter by the power of six. This means that even in very low numbers the size of large particles d_{geo} derived by Eq. (4) is

overrepresented against slightly smaller ones [52]. For Ti-E, the calculated diameter $d_{geo} = 77$ nm aligns well with the maximum particle size observed in the number density distribution derived by TEM (Fig. 1b).

In both cases, the marked slope in gray is lower than the one for the small particles in blue: 3.2 for Ti-S and 2.8 for Ti-E. Here, the scattering information about the aggregate and the large particles are overlapping resulting in a mix of surface fractal of the large particles and mass fractal of the aggregates. Although there are fewer large particles in Ti-S, their impact on the scattering is stronger due to their large size. The slope of the aggregates (purple lines) appears for the two samples at different places in the scattering data. For Ti-E, the mass fractal of the aggregates is detected at the smallest scattering vectors crossing from the SAXS to the USAXS region. This is expected as the size of the aggregates is assumed larger than any particles. The derived value of 1.7 for the fractal dimension of mass is in good agreement with other theoretical and experimental results [56–58]. However, no size for the aggregates could be derived. A possible reason could be a very wide distribution in size, where the largest share might be out of bounds for the smallest detectable scattering vector. In contrast, the mass fractal of Ti-S $p = 2.3$ can be detected between the two Guinier areas due to the larger difference in size between the small and large particle fraction. This value ($p = 2.3$) might be influenced by the surface fractal of the large particle leading to a higher value as reported in literature.

In addition to the concentration of 0.5 mol L^{-1}, precursor compositions of 1.0 mol L^{-1} and 1.5 mol L^{-1} were combusted in each burner setup. The results are close to the presented data in Fig. 1 with distinct differences. Fig. 2a shows the calculated particle size (small in blue, large in gray) in dark colors for Ti-S and light colors for Ti-E. The small particles increase slightly in size with increasing concentration, stronger for Ti-S ($d_{mean} = 8$–18 nm) than for Ti-E ($d_{mean} = 8$–14 nm). In contrast, the large particles of Ti-E double in diameter from $d_{geo} = 75$ nm to $d_{geo} = 145$ nm while the precursor concentration triples. For Ti-S, we expect a similar increase for the large particle fraction. Apart from the calculated diameter $d_{geo} = 183$ nm for a concentration of 0.5 mol L^{-1}, these sizes would be beyond the scope of the Bonse-Hart module.

Fig. 2b depicts the development of the different fractal dimensions with precursor concentration. The surface fractal of the small particles stays close to four representing smooth surfaces. The slope p for the large particles ranges between 2.7 and 3.7. As the size increases with the concentration so does the value of the slope p because the influence of the scattering of the aggregates lessens. In turn, the dimension of mass for Ti-S decreases with increasing concentration assuming a value of 1.75 in agreement with literature [57,58]. This points to less overlap of scattering between the large particles and the mass fractals of the aggregates. It confirms the earlier assumption of an increase of the large particle size with increasing concentration. For Ti-E, the fractal dimension of mass is fluctuating around $p = 1.6$–2.

Overall, both particle systems show similar characteristics with increasing precursor concentration albeit the size of the larger particles differs greatly. The gas-to-particle pathway is highly likely responsible for the formation of the small particle fraction. Their observed size increases slightly with increasing precursor concentration and is almost independent of burner setup. The larger particles might stem from the droplet-to-particle pathway. This would mean the droplet size of the spray is responsible for the size of the resulting particle. However, for particles solely formed by the droplet-to-particle pathway, a particle size in submicron to micron range is expected [4]. A more plausible explanation might be hydrolysis reactions of the precursor in the droplet. This could lead to molecule clusters bevor the evaporation thus resulting in larger particles.

To gain a deeper insight into how these particles develop, *in situ* measurements through and above the flame were conducted at the synchrotron KARA (selected SAXS data in the supplement in Fig. 3S). Fig. 3a shows the development of the small particle fraction with increasing height above the burner (HAB) for Ti-S with a precursor concentration of 0.5 mol L^{-1} (dark blue) and 1.0 mol L^{-1} (light blue). The results of Fig. 2 are included as "*ex situ*" (last data point in Fig. 3) for both concentrations. For 0.5 mol L^{-1}, a nearly constant particle size of $d_{mean} \approx 6$ nm is measured at all HAB and for the *ex situ* sample. Already at 5 mm above the burner, particles were detected. As mentioned above, we presume that these small particles result from the gas-to-particle pathway: The precursor evaporates in the gas phase and the particle formation begins with nucleation. After they turn from molecule clusters to solid particles, they do not seem to grow anymore in size. This changes with a higher precursor concentration of 1.0 mol L^{-1}. The particles double in size from 6 nm to 12 nm if the first calculated diameter at 10 mm HAB is compared to the *ex situ* result. This growth in size can only be explained by the higher precursor concentration, which is also evident in the *ex situ* results.

Fig. 3b shows surface fractals at small HABs in black and gray for a

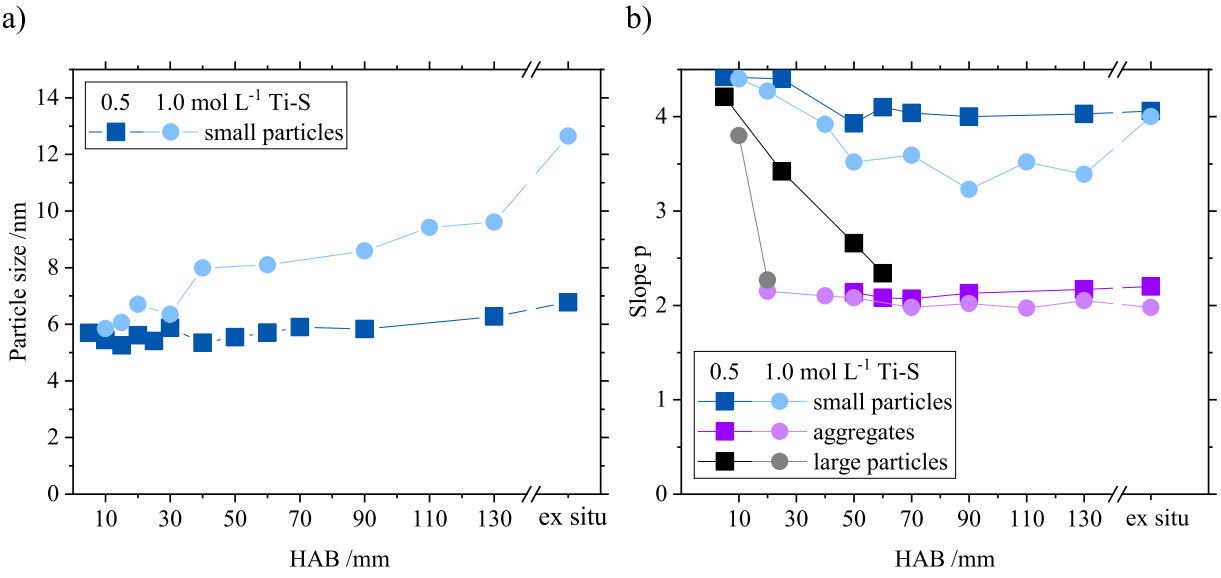

Fig. 3. SAXS results for Ti-S at different heights above the burner (HAB) from *in situ* experiments at KARA. (a) Particle size: d_{mean} (Eq. (5)). (b) Slope p for small particles (surface fractal), aggregates (mass fractal) and large particles (surface fractal). (For interpretation of the references to color in this figure legend, the reader is referred to the web version of this article.)

precursor concentration of 0.5 mol L^{-1} and 1.0 mol L^{-1} respectively. These were identified at the smallest scattering vectors (see Fig. 3S). The slope p decreases from 4 (meaning smooth surfaces) to below 3 with increasing distance from the burner. Since values below 3 are not physically possible for surface fractals, this could point to mass fractals of large particles beyond the resolution of the *in situ* SAXS. A growth of the large particles would shift the Guinier region for their size to even smaller scattering vectors. This theory is supported by Aßmann et al. who investigated the same precursor (TTIP) in ethanol at 0.1 mol L^{-1} using *in situ* wide angle light scattering (WALS) measurements. For the large particles (spheres), they showed a growth of 14% from 96 – 133 nm at 50 - 120 mm HAB [39].

With increasing HAB, the number of aggregates formed by collision of particles and agglomeration should increase as well. Almost at the same HAB, where the surface fractals disappear, mass fractals for aggregates are visible (in purple). This shift happens at a HAB of 50–60 mm for a concentration of 0.5 mol L^{-1} and at HAB of 20 mm for 1.0 mol L^{-1}. The mass fractals stay at values around 2 throughout the *in situ* measurements and the *ex situ* sample for both concentrations. In contrast, the surface fractals of the small particles (in blue) vary greatly. This fluctuation is probably a result of the low signal-to-noise of the data at the largest detected scattering vectors.

Although the *in situ* experiments cannot point to the origin of the large particles, they confirm the assumption of the gas-to-particle pathway. Particles were detected as low as 5 mm above the burner with a size of almost 6 nm. The data shows the growth of these small particles as well as their aggregation.

For titanium oxide nanoparticles made in a spray flame, our experiments reveal the bimodality of the primary particle distribution as well as the mass fractals of the aggregates. The details of the TEM particle

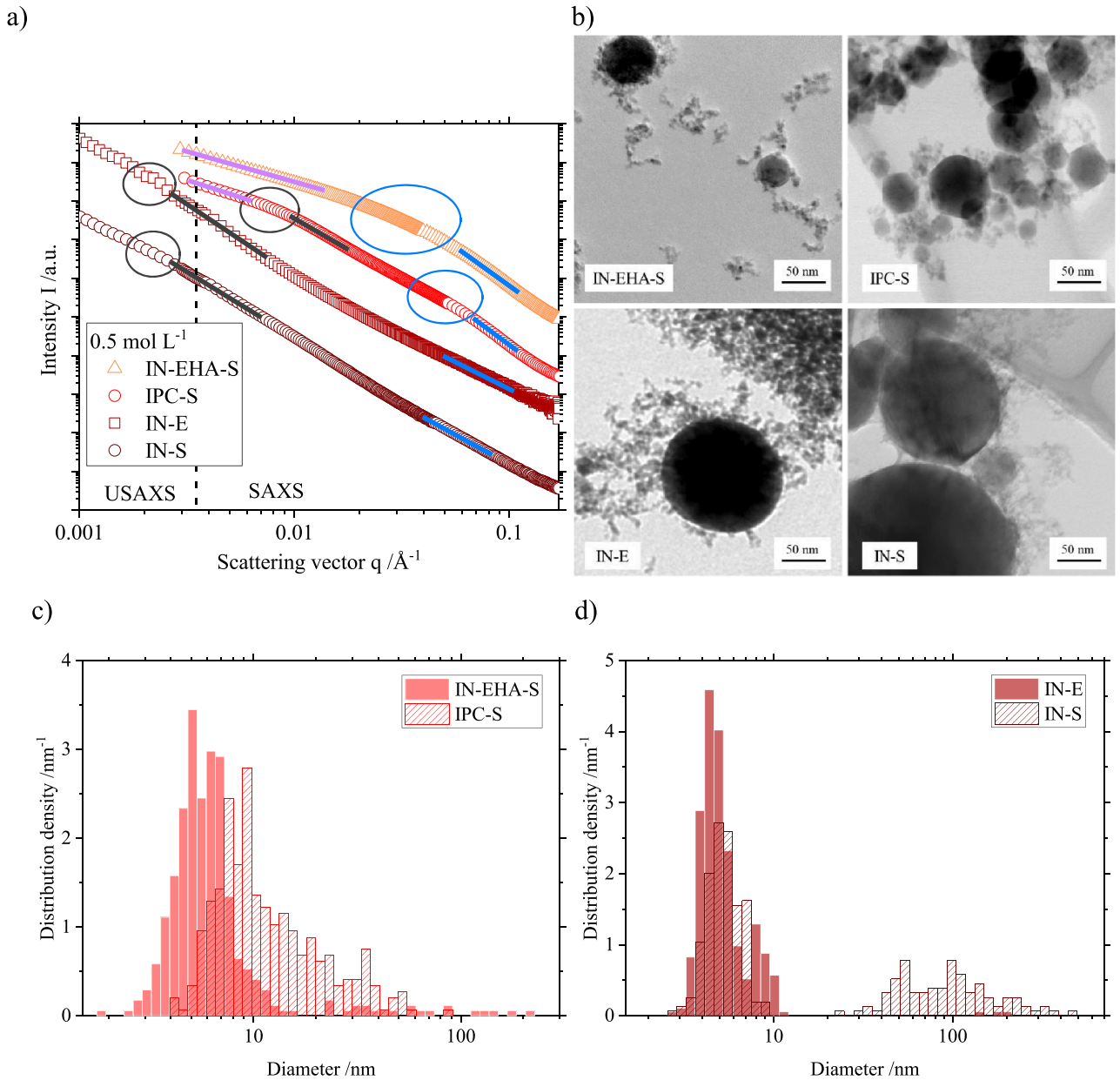

Fig. 4. Samples IN-EHA-S, IPC-S, IN-E and IN-S with concentration of 0.5 mol L^{-1} (IN: iron nitrate nonahydrate, IPC: iron pentacarbonyl, EHA: 2-ethylhexanoic acid). (a) (U)SAXS data including markings for the Guinier (circles) and power (lines) laws (blue = small particles, gray = large particles, purple = aggregates). (b) Exemplary TEM images. (c) Number density distributions derived from TEM for IN-EHA-S and IPC-S. (d) Number density distributions derived from TEM for IN-E and IN-S. (For interpretation of the references to color in this figure legend, the reader is referred to the web version of this article.)

characterization lead to the assumption of the gas-to-particle pathway as the main particle formation mechanism in regards to the number of particles. The few large particles might result from hydrolysis of the precursor in the droplets before they evaporate. This mechanism could be described as a model between the droplet-to-particle and gas-to-particle pathway.

3.2. Iron oxide

In order to understand the influence of the material system on the particle structure, similar experiments were conducted with iron oxide nanoparticles. The same two burner setups *SpraySyn1* (S) and electrospray (E) were used with different precursors compositions: iron pentacarbonyl in ethanol (IPC), iron nitrate in ethanol or isopropanol (IN) and iron nitrate in 65% 2-ethylhexanoic acid and 35% ethanol (IN-EHA). Fig. 4a depicts the SAXS results of the powder samples IN-EHA-S, IPC-S, IN-E and IN-S with a precursor concentration of 0.5 mol L^{-1} as data points in red colors including markings for the Guinier and power law fits. For better readability, the scattering curves are stacked in arbitrary units. Fig. 4b shows an exemplary TEM image for each particle system with the same magnification. All samples consist of aggregate structures of very small particles and some larger particles in a wide range of sizes. The resulting number density distributions derived from TEM are displayed in Fig. 4c and Fig. 4d.

Starting with iron nitrate nonahydrate (IN) in pure alcohol, the results for the *SpraySyn1* burner (IN-S) and setup for SFS with electrospray (IN-E) are similar: In both cases, USAXS yields a Guinier region for the large particle fraction: d_{geo}≈300 nm for IN-S and d_{geo}≈320 nm for IN-E. The TEM images (Fig. 4b) confirm this claim with a few large particles in the same order of magnitude. The size distributions of the TEM analysis (Fig. 4d) reveal a higher number of large particles for IN-S than IN-E in a very broad size range. Similar to the SAXS results of Ti-S, the largest particles are overrepresented in the calculated diameter d_{geo} for IN-S and IN-E. As discussed in the introduction, hydrolysis in the precursor solution promotes the precipitation of iron oxide and could lead to larger particles. The corresponding power law fits (gray line) reveal a slope p with values higher 3 pointing to surface fractals of the larger particles which are influenced by the mass fractals of the aggregates. However, the TEM images and number density distributions show plenty of very small particles around 5 nm exist as well similar to Ti-S (Fig. 1b). Therefore, the scattering of the few large particles overpowers any other scattering. No Guinier region of the smaller particles can be detected at larger scattering vectors. Similarly, the power law fit for the small particles (blue line) yields slope $p < 3$ in both cases which is physically not feasible.

For IPC-S, the circles mark the Guinier region for small particles of d_{mean}≈5 nm in blue and the larger ones of d_{geo}≈60 nm in gray (see Fig. 4a). These sizes are in good agreement with the TEM image (Fig. 4b). The number density distribution in Fig. 4c cannot corroborate a clear bimodality but shows a slight slump at the diameters just below 30 nm. The surface of the small particles is nearly smooth (blue line with $p = 4.1$). The transition between the two Guinier regions is a mix of surface fractals of the larger particles and mass fractals of the aggregates. The highest value for p with 3.1 is marked with a gray line close to the Guinier region of the large particle fraction. At the smallest scattering angles, the mass fractal of the aggregates reaches a value of $p = 1.75$. The results are in good agreement for flame-made aggregates as reported in literature [57,58].

The addition of EHA inhibits the formation of iron-hydroxides in the precursor solution with IN, which influences the particle formation process in the flame. The result is a typical structure for flame-made aggregates as shown for IN-EHA-S in Fig. 4a: primary particles with a size of ~6 nm and slightly rough surfaces ($p = 3.9$) and a fractal dimension of mass of 1.6 for the aggregates. The very gradual change in slope points to a broad distribution of the primary particles. These findings are only partially in agreement with the exemplary TEM image in Fig. 4b. In addition to the small particles, 2 larger particles of under 50 nm are present. This bimodality of the primary particles is observed in the number density distribution in Fig. 4c. Tischendorf et al. confirmed the described structure albeit at a concentration of 0.1 mol L^{-1} [26]. One reason, why these larger particles cannot be identified as a separate Guinier region with SAXS could be a very broad size distribution from 25 to 200 nm.

The occurrence and number of larger particles may not only depend on the precursor but also on the concentration. Therefore, a different range of concentrations of each precursor was investigated. The calculated particle and aggregate sizes from the SAXS data is displayed in Fig. 5a in the established color code. For IPC-S, the aforementioned bimodal particle distribution with a small and large particle fraction is identified for all investigated precursor concentrations. The small particles stay in the order of magnitude of 5 to 8 nm whereas the size of the large particles increases with increasing concentration (d_{geo} = 30–65 nm). The same behavior was observed for titanium oxide prepared from electrospray (Ti-E).

However, the results for electrospray with iron nitrate (IN-E) differ greatly from Ti-E. For IN-E, USAXS measurements reveal particle sizes of d_{geo} = 250–320 nm for the large particle fraction in the investigated range of precursor concentrations of 0.5 – 1.5 mol L^{-1}. Contrary to the results discussed until this point, the size of the large particles decreases with increasing concentration. For IN-S, the USAXS results reveal a similar size range for the large particles as observed for IN-E. Here, the particle size increases from 200 nm at 0.1 mol L^{-1} to 300 nm at 0.5 mol L^{-1}. For both precursor compositions, TEM analysis shows a consistent size of around 5 nm across the studied concentration range. This is not visible in the SAXS data due to the scattering of the large particles. Through the addition of EHA to the precursor solution (IN-EHA-S), SAXS reveals the small particle fraction for all measured concentrations. The size is in the same range as all other samples (d_{mean} = 5–8 nm), further cementing the hypothesis of a gas-to-particle pathway as main particle formation process.

In addition to the size, the fractal properties were also investigated. Fig. 5b compares the different values of the slope p for IPC-S and IN-EHA-S. The surface fractals of the small primary particles show contrary trends but end up with a sharp interface ($p = 4$) at the highest concentration investigated. For IPC-S, the values decrease below 4 whereas for In-EHA-S p increases to 4.

The change of the slope p for the large particles of IPC-S is the strongest observed in this study. Similar to TI-S and Ti-E, the slope p increases with increasing precursor concentration. At 0.2 mol L^{-1}, the slope $p = 2.8$ is between a mass and surface fractal. This is likely a result of the close sizes of small and large particle fraction (see Fig. 5a). The slope p reaches the value 4 at a concentration of 0.8 mol L^{-1} showing Porod behavior [53]. Here, the mass fractals have no impact on the surface fractals which may be a result of a higher number of large particles.

Concerning the aggregates, the fractal dimension of mass decreases slightly for both precursor compositions. IPC-S starts with a value of 2 at 0.2 mol L^{-1} and stays at 1.75 for the other two investigated concentrations which points to diffusion-limited cluster aggregation. This is typical for flame-made aggregates and also extends to the results of IN-EHA-S. Here, the range for $p = 1.6 – 1.8$ is lightly larger than described in the literature (1.7 – 1.8) [57,58]. A higher precursor concentration would lead to more particles in the flame if the particle size does not increase significantly. In turn, more particles result in a higher collision frequency and consequently in highly branched aggregates with lower values for the fractal dimension of mass.

The details presented in Fig 5 show the potential and shortcomings of SAXS at the same time. The gain of information about the particle structure covers multiple characteristics like different particle sizes and fractal dimensions. However, overlap of information can obscure important particle properties as shown in IN-S and IN-E in Fig. 4a. This extensive comparison of different iron oxide precursors reveals the

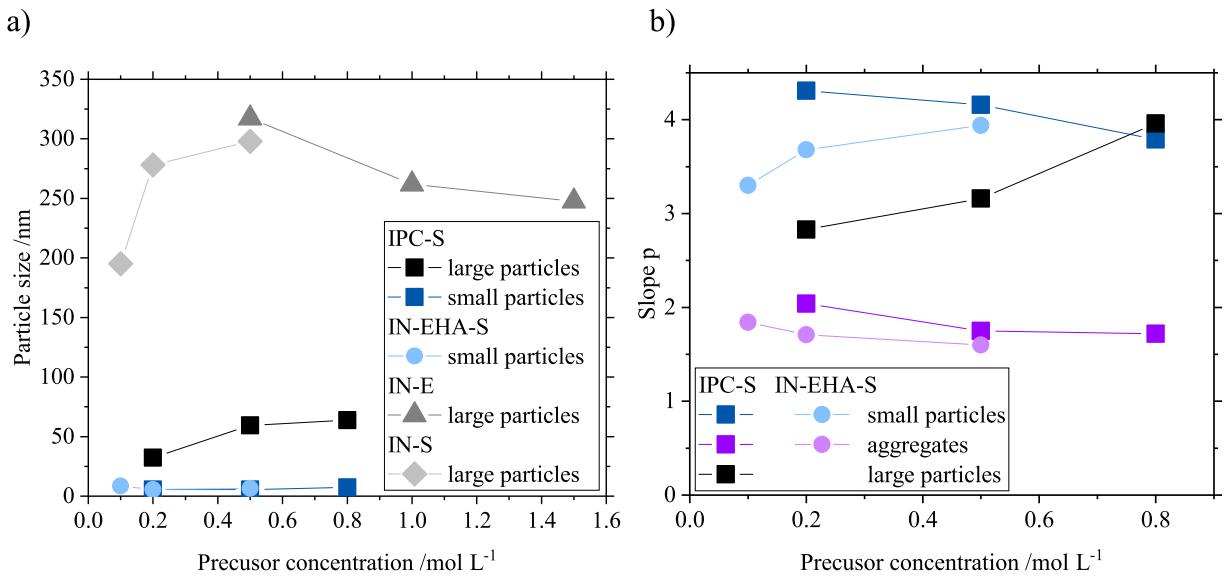

Fig. 5. SAXS results for IPC-S, IN-EHA-S, IN-E and IN-S at different iron concentrations. (a) Particle size: large particles: d_{geo} (Eq. (4)). Small particles: d_{mean} (Eq. (5)). (b) Slope p for small particles (surface fractal), aggregates (mass fractal) and large particles (surface fractal). (For interpretation of the references to color in this figure legend, the reader is referred to the web version of this article.)

impact of precursor concentration, solvent composition and burner setup. Trends are certainly detectable as well as exceptions: the small particles hardly change size independent of the mentioned variations in production because they doubtless are a result of the gas-to-particle pathway. In contrast, the characteristics of the large particles strongly depend on the material properties of the precursor solution suggesting a chemical reaction of the precursor. As explained for titanium oxide, the formation of these large particles might start in the droplet and end in the gas phase combining both pathways.

To ensure the claim of the gas-to-particle pathway for iron oxide, *in situ* investigations of IN-EHA-S were conducted using TS-TEM in Paderborn and synchrotron radiation at KARA in Karlsruhe. IN-EHA-S with a precursor concentration of 0.1 mol L^{-1} is the defined standard system of the SPP1980 *SpraySyn*. Fig. 6 shows exemplary TEM-images of particles extracted at different heights above the burner with the same magnification. More images gained by the *in situ* extraction are provided in the supplement (Fig. 4Sb). At HAB 50 mm, particles of only a few nanometers could be extracted as well as a crystal with a size of around 10 nm. Here, no signs of aggregation are visible. At HAB 100 mm, the image displays part of an aggregate consisting of crystals. The particle

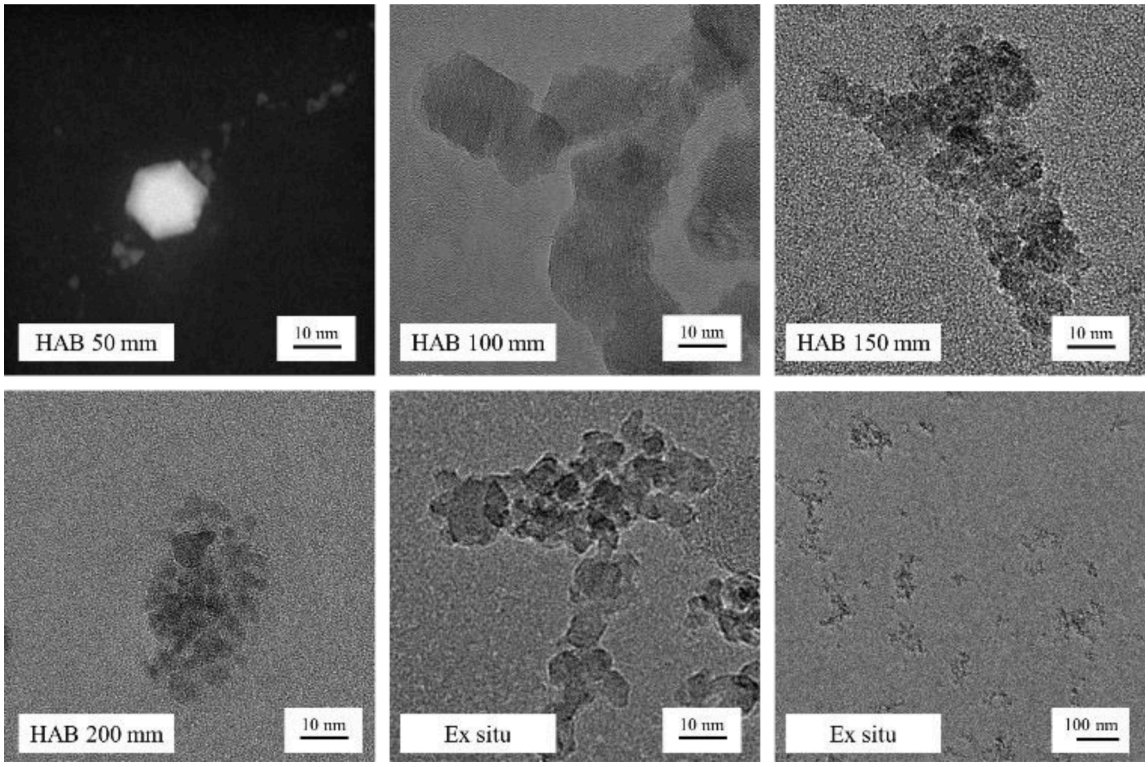

Fig. 6. TEM images of IN-EHA-S (0.1 mol L^{-1}) at different HAB (extracted *in situ*) and of powder samples (*ex situ*).

structure does not change significantly from HAB 150 mm to 200 mm showing a small aggregate consisting of small particles of under 5 nm. Images gained from the powder sample (*ex situ*) reveal primary particles of the same size. The aggregate size seems to be under 100 nm with a shape typical for flame-made products. These *ex situ* results are in very good agreement with the presented SAXS data of the particle system in Fig. 5. Here, a similar size was derived for primary particles as well as the fractal dimension of mass of 1.8 for the form of the aggregate.

For the *in situ* experiments with SAXS, Fig. 7a shows the evolution of the primary particles while Fig. 7b depicts the changes in the different fractal dimensions. The associated SAXS scattering can be found in the supplement (Fig. 4Sa). The results of Fig. 5 for IN-EHA serve as "*ex situ*" sample (last data point in Fig. 7). Starting at HAB 30 mm, the size detected for the particles is around 4 nm (see Fig. 7a). From there the particles grow to 5 nm and stay that size up to HAB 190 mm. The *ex situ* sample yields $d_{mean} = 8$ nm representing the average size of all particles including the larger crystals.

Fig. 7b shows the evolution of the different fractal dimension. The fractal dimension of mass (purple) decreases from 2.4 to 1.8 describing a change in the aggregate from a denser and flatter to a looser and stringier shape. This evolution could point to a growth of the aggregate in size. A small aggregate of only a few particles can only form a dense shape compared to a larger one of many primary particles. The surface fractal of the primary particles changes from over 4 to 3.5. This is a result of the low signal-to-noise at the large scattering vectors. Starting at HAB 150 mm, the rough surface derived from values of around $p = 3.5$ are in good agreement with the TEM images (see Fig. 6). Here, the particles appear round with some corners or edges. A second fractal dimension of surface (black) was detectable at small scattering angles. The slope p decreases with more distance to the burner from almost 4 to below 3.

Usually, this fact points to larger particles. In this case, we know that large particles exist neither in the *in situ* nor *ex situ* TEM images of Fig. 6 or in *ex situ* SAXS of Fig. 5. It could be an indication for precursor droplets. We expect more droplets closer to the burner and more particles in form of aggregates above the flame leading to a weaker influence of the droplets with increasing HAB. Similarly, droplets could be a possible explanation for the surface fractals detected for Ti-S at small scattering angles (Fig. 3b). However, *ex situ* SAXS and TEM images prove the presence of large particles in both concentrations of Ti-S. Additionally, EHA has a very high boiling point of over 200 °C in contrast to isopropanol with 82 °C leading to droplets high above the flame and residue of EHA in the exhaust.

4. Conclusion

For complex aggregate structures made by spray flame synthesis, the combination of SAXS measurements with TEM analysis proves to be a powerful tool revealing a multitude of information about the particle size and morphology. In this study, the primary particles show a bimodal distribution independent of the precursor compositions and burner setups. With SAXS, the size of both particle fractions and the aggregates' fractal dimension of mass were identified. Without exception, the small primary particles stay in the range of 5–10 nm indicating a formation via the gas-to-particle pathway. *In situ* measurements using synchrotron radiation confirm this hypothesis. Number density distributions derived from TEM show the small particles as the bigger fraction thus corroborating the gas-to particle pathway as the main mechanism. The quantity and size of the large particle fraction depend on the chemical properties of precursor solution suggesting chemical reactions of the precursor in the droplets of the spay.

The bimodality for Ti-E and IPC-S is characterized in the scattering curve with 2 Guinier areas quite close together connected with a mixed fractal dimension of surface and mass. For increased quantities or increased sizes of the large particle fraction, as observed for In-E and IN-S, the scattering from the fractal dimension of surface overlaps with the Guinier region of the small particle fraction.

For all precursor compositions, an increase in the concentration only slightly increases the size of the small particle fraction. The large particles tend to strongly increase in size apart from IN-E. With increasing concentration, the mix of mass and surface fractals shifts to clear surface fractals of the large particles: the slope p increase to the value 4 pointing to smooth surfaces with a sharp interface (Porod behavior). The fractal dimension of mass reaches a value of 1.6–1.75 at the highest investigated concentration. These values indicate diffusion-limited cluster aggregation which is typical for flame-made products.

The production of metal oxide nanoparticles via spray flame synthesis is a promising approach for large scale industrial manufacture of highly pure aggregates with a large specific surface. However, chemical reactions in precursor solutions and details of the burner setup influence the particle formation leading to a highly polydisperse product. SAXS

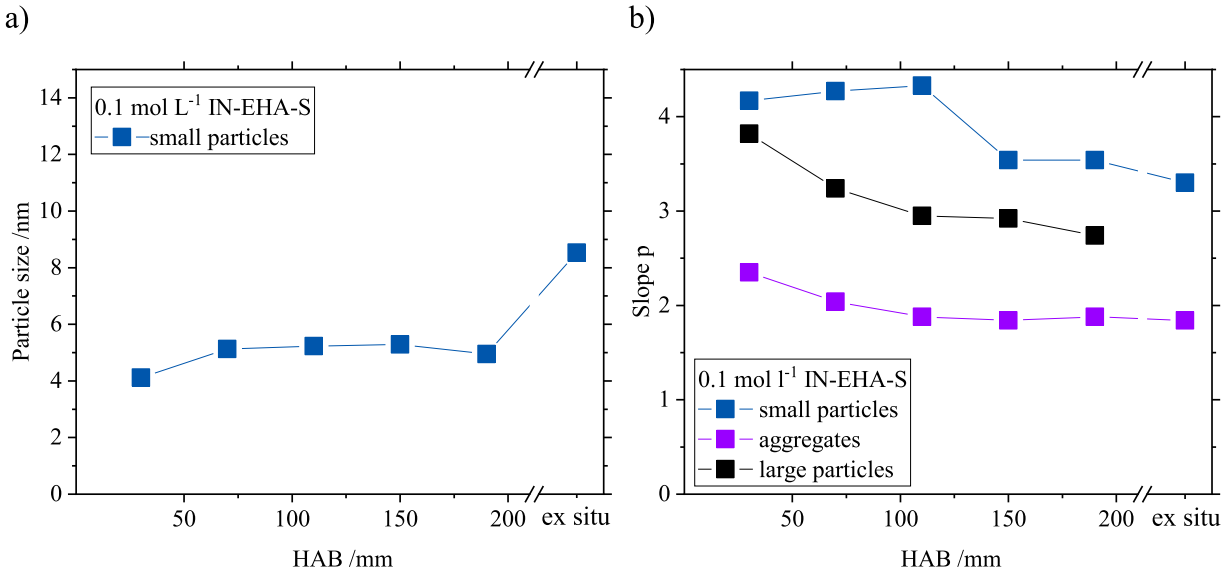

Fig. 7. SAXS results for IN-EHA-S at different heights above the burner (HAB) from *in situ* experiments at KARA. (a) Particle size: d_{mean} (Eq. (5)). (b) Slope p for small particles (surface fractal), aggregates (mass fractal) and large particles (surface fractal). (For interpretation of the references to color in this figure legend, the reader is referred to the web version of this article.)

provides detailed information about the bimodality of the primary particles and shape of the aggregates. This leads to the assumption of a pure gas-to-particle pathway for the fraction of the small particle. The formation of large particles might start with hydrolysis reactions of the precursor and forming of molecule clusters in the droplet followed by solidifying to particles (droplet-to-particle). The rest of the precursor in the droplet could evaporate into the gas phase (gas-to-particle). With consistent measurements, the parameters for production can be optimized for the intended functional properties of the particles.

Declaration of Competing Interest

The authors declare that they have no known competing financial interests or personal relationships that could have appeared to influence the work reported in this paper.

Data availability

Data will be made available on request.

Acknowledgements

The research leading to these results has received funding from the German Research Foundation (DFG) within the priority program SPP 1980 *SpraySyn* (Ni 414/30-1, Ni 414/30-2, SCHM 1429/13-1 and WE 2331/20-1).

We acknowledge provision of beam time and would like to thank Anton Plech and Gernot Buth for their assistance during the experiments as well as the Institute for Beam Physics and Technology (IBPT) for the operation of the storage ring, the Karlsruhe Research Accelerator (KARA).

We would like to thank Abhijeet Kumar for the production of the powder samples from IPC-ethanol solutions using the *SpraySyn1* burner at the Otto-von-Guericke University of Magdeburg.

Supplementary materials

Supplementary material associated with this article can be found, in the online version, at doi:10.1016/j.jaecs.2023.100183.

References

[1] Teoh WY, Amal R, Mädler L. Flame spray pyrolysis: an enabling technology for nanoparticles design and fabrication. Nanoscale 2010;2:1324–47. https://doi.org/10.1039/C0NR00017E.
[2] Strobel R, Baiker A, Pratsinis SE. Aerosol flame synthesis of catalysts. Adv Powder Technol 2006;17:457–80. https://doi.org/10.1163/156855206778440525.
[3] Li S, Ren Y, Biswas P, Tse SD. Flame aerosol synthesis of nanostructured materials and functional devices: processing, modeling, and diagnostics. Prog Energy Combust Sci 2016;55:1–59. https://doi.org/10.1016/j.pecs.2016.04.002.
[4] Purwanto A, Wang W-N, Okuyama K. Flame Spray Pyrolysis. In: Ashgriz N, editor. Handbook of atomization and sprays: theory and applications. Boston, MA: Springer Science+Business Media LLC; 2011. p. 869–79.
[5] Strobel R, Pratsinis SE. Flame aerosol synthesis of smart nanostructured materials. J Mater Chem 2007;17:4743. https://doi.org/10.1039/b711652g.
[6] Pawłowski L, Blanchart P. Industrial chemistry of oxides for emerging applications. Chichester, UK: John Wiley & Sons Ltd; 2018.
[7] Guo Q, Zhou C, Ma Z, Yang X. Fundamentals of TiO2 Photocatalysis: concepts, Mechanisms, and Challenges. Adv Mater 2019;31:e1901997. https://doi.org/10.1002/adma.201901997.
[8] Chiarello GL, Selli E, Forni L. Photocatalytic hydrogen production over flame spray pyrolysis-synthesised TiO2 and Au/TiO2. Appl Catal B 2008;84:332–9. https://doi.org/10.1016/j.apcatb.2008.04.012.
[9] Huber DL. Synthesis, properties, and applications of iron nanoparticles. Small 2005;1:482–501. https://doi.org/10.1002/smll.200500006.
[10] Sodipo BK, Aziz AA. Recent advances in synthesis and surface modification of superparamagnetic iron oxide nanoparticles with silica. J Magn Magn Mater 2016;416:275–91. https://doi.org/10.1016/j.jmmm.2016.05.019.
[11] Chatterjee J, Haik Y, Chen C-J. Size dependent magnetic properties of iron oxide nanoparticles. J Magn Magn Mater 2003;257:113–8.
[12] Gupta AK, Gupta M. Synthesis and surface engineering of iron oxide nanoparticles for biomedical applications. Biomaterials 2005;26:3995–4021. https://doi.org/10.1016/j.biomaterials.2004.10.012.
[13] Grimm S, Schultz M, Barth S, Muller R. Flame pyrolysis – a preparation route for ultrafine pure γ-Fe2O3 powders and the control of their particle size and properties. J Mater Sci 1997;32:1083–92. https://doi.org/10.1023/A:1018598927041.
[14] Strobel R, Pratsinis SE. Direct synthesis of maghemite, magnetite and wustite nanoparticles by flame spray pyrolysis. Adv Powder Technol 2009;20:190–4. https://doi.org/10.1016/j.apt.2008.08.002.
[15] Li D, Teoh WY, Selomulya C, Woodward RC, Munroe P, Amal R. Insight into microstructural and magnetic properties of flame-made γ-Fe2O3 nanoparticles. J Mater Chem 2007;17:4876. https://doi.org/10.1039/b711705a.
[16] Jossen R, Pratsinis SE, Stark WJ, Madler L. Criteria for flame-spray synthesis of hollow, shell-like, or inhomogeneous oxides. J Am Ceramic Soc 2005;88:1388–93. https://doi.org/10.1111/j.1551-2916.2005.00249.x.
[17] Meierhofer F, Li H, Gockeln M, Kun R, Grieb T, Rosenauer A, Fritsching U, Kiefer J, Birkenstock J, Mädler L, Pokhrel S. Screening precursor-solvent combinations for Li4Ti5O12 energy storage material using flame spray pyrolysis. ACS Appl Mater Interfaces 2017;9:37760–77. https://doi.org/10.1021/acsami.7b11435.
[18] Li H, Rosebrock CD, Riefler N, Wriedt T, Mädler L. Experimental investigation on microexplosion of single isolated burning droplets containing titanium tetraisopropoxide for nanoparticle production. Proc Combust Inst 2017;36:1011–8. https://doi.org/10.1016/j.proci.2016.09.017.
[19] Jeon JB, Kim BJ, Bang GJ, Kim M-C, Lee DG, Lee JM, Lee M, Han HS, Boschloo G, Lee S, Jung HS. Photo-annealed amorphous titanium oxide for perovskite solar cells. Nanoscale 2019;11:19488–96. https://doi.org/10.1039/c9nr05776e.
[20] Leaustic A, Babonneau F, Livage J. Structural investigation of the hydrolysis-condensation process of titanium alkoxides Ti(OR)4 (OR = OPr-iso, OEt) modified by acetylacetone. 1. Study of the alkoxide modification. Chem. Mater. 1989;1:240–7. https://doi.org/10.1021/CM00002A015.
[21] Schwertmann U, Cornell RM. Iron oxides in the laboratory: preparation and characterization. John Wiley & Sons; 2008.
[22] Cornell RM, Schwertmann U. The iron oxides: structure, properties, reactions, occurrences, and uses, secondnd, completely rev. and extended ed. Weinheim: WILEY-VCH; 2003.
[23] Stodt MFB, Gonchikzhapov M, Kasper T, Fritsching U, Kiefer J. Chemistry of iron nitrate-based precursor solutions for spray-flame synthesis. Phys Chem Chem Phys 2019;21:24793–801. https://doi.org/10.1039/c9cp05007h.
[24] Keller A, Wlokas I, Kohns M, Hasse H. Thermophysical properties of solutions of iron(III) Nitrate nonahydrate in mixtures of 1-propanol and water. J Chem Eng Data 2020;65:5413–20. https://doi.org/10.1021/acs.jced.0c00531.
[25] Keller A, Wlokas I, Kohns M, Hasse H. Thermophysical properties of solutions of iron(III) nitrate-nonahydrate in mixtures of ethanol and water. J Chem Eng Data 2020;65:3519–27. https://doi.org/10.1021/acs.jced.0c00105.
[26] Tischendorf R, Simmler M, Weinberger C, Bieber M, Reddemann M, Fröde F, Lindner J, Pitsch H, Kneer R, Tiemann M, Nirschl H, Schmid H-J. Examination of the evolution of iron oxide nanoparticles in flame spray pyrolysis by tailored *in situ* particle sampling techniques. J Aerosol Sci 2021;154:105722. https://doi.org/10.1016/j.jaerosci.2020.105722.
[27] Angel S, Neises J, Dreyer M, Friedel Ortega K, Behrens M, Wang Y, Arandiyan H, Schulz C, Wiggers H. Spray-flame synthesis of La(Fe, Co)O 3 nano-perovskites from metal nitrates. AIChE J 2020;66:441. https://doi.org/10.1002/aic.16748.
[28] Angel S, Schneider F, Apazeller S, Kaziur-Cegla W, Schmidt TC, Schulz C, Wiggers H. Spray-flame synthesis of LaMO3 (M= Mn, Fe, Co) perovskite nanomaterials: effect of spray droplet size and esterification on particle size distribution. Proc Combust Inst 2021;38:1279–87.
[29] Angel S, Tapia JD, Gallego J, Hagemann U, Wiggers H. Spray-flame synthesis of LaMnO 3+δ nanoparticles for selective CO oxidation (SELOX). Energy Fuels 2021;35:4367–76. https://doi.org/10.1021/acs.energyfuels.0c03659.
[30] Gonchikzhapov M, Kasper T. Decomposition reactions of Fe(CO) 5 Fe(C 5 H 5) 2 and TTIP as precursors for the spray-flame synthesis of nanoparticles in partial spray evaporation at low temperatures. Ind Eng Chem Res 2020;59:8551–61. https://doi.org/10.1021/acs.iecr.9b06667.
[31] Karakaya Y, Kluge S, Wiggers H, Schulz C, Kasper T. Investigation of the combustion of iron pentacarbonyl and the formation of key intermediates in iron oxide synthesis flames. J Appl Phys 2021;230:116169. https://doi.org/10.1016/j.ces.2020.116169.
[32] Bonse U, Hart M. Tailless X-ray single-crystal reflection curves obtained by multiple reflection. Appl Phys Lett 1965;7:238–40. https://doi.org/10.1063/1.1754396.
[33] Bonse U, Hart M. Small angle X-ray scattering by spherical particles of Polystyrene and Polyvinyltoluene. Z Physik 1966;189:151–62. https://doi.org/10.1007/BF01327152.
[34] Gröhn AJ, Eggersdorfer ML, Pratsinis SE, Wegner K. On-line monitoring of primary and agglomerate particle dynamics. J Aerosol Sci 2014;73:1–13. https://doi.org/10.1016/j.jaerosci.2014.03.001.
[35] Mohammadi S, Poostforooshan J, Stodt MF, Olszok V, Kiefer J, Fritsching U, Weber AP. Tailoring crystal structure and morphology of MnOx nanoparticles via electrospray-assisted flame spray pyrolysis. Appl Energy Combust Sci 2023:100151. https://doi.org/10.1016/j.jaecs.2023.100151.
[36] Suleiman S, Nanjaiah M, Skenderovic I, Rosenberger T, Kunze F, Wlokas I, Kruis FE, Wiggers H, Schulz C. Atmospheric-pressure particle mass spectrometer for investigating particle growth in spray flames. J Aerosol Sci 2021;158:105827.

[37] Zhao B, Yang Z, Wang J, Johnston MV, Wang H. Analysis of soot nanoparticles in a laminar premixed ethylene flame by scanning mobility particle sizer. Aerosol Sci Technol 2003;37:611–20. https://doi.org/10.1080/02786820300908.
[38] Lee J, Altman I, Choi M. Design of thermophoretic probe for precise particle sampling. J Aerosol Sci 2008;39:418–31. https://doi.org/10.1016/j.jaerosci.2008.01.001.
[39] Aßmann S, Münsterjohann B, Huber FJT, Will S. In situ determination of droplet and nanoparticle size distributions in spray flame synthesis by wide-angle light scattering (WALS). Materials (Basel, Switzerland) 2021:14. https://doi.org/10.3390/ma14216698.
[40] Stodt MFB, Liu C, Li S, Maedler L, Fritsching U, Kiefer J. Phase-selective laser-induced breakdown spectroscopy in flame spray pyrolysis for iron oxide nanoparticle synthesis. Proc Combust Inst 2021;38:1711–8.
[41] R. Jossen, Controlled synthesis of mixed oxide nanoparticles by flame spray pyrolysis, 2006.
[42] M. Simmler, M. Meier, L. Rank, G. Buth, A. Plech, H. Nirschl, Beamline setup for *in situ* measurements of particles in turbulent spray flames using small angle X-ray scattering, Proceedings of the Combustion Institute (2022) under Review.
[43] Simmler M, Meier M, Nirschl H. Characterization of fractal structures by spray flame synthesis using X-ray scattering. Materials (Basel, Switzerland) 2022:15. https://doi.org/10.3390/ma15062124.
[44] Schneider F, Suleiman S, Menser J, Borukhovich E, Wlokas I, Kempf A, Wiggers H, Schulz C. SpraySyn-A standardized burner configuration for nanoparticle synthesis in spray flames. Rev Sci Instrum 2019;90:85108. https://doi.org/10.1063/1.5090232.
[45] Bierwirth M, Olszok V, Ganesan VA, Poostforooshan J, Weber AP. Analyse der partikelbildung aus der elektrospray-flammensprühpyrolyse mittels scanning mobility particle sizer. Chem Ingenieur Technik 2021;93:1307–15. https://doi.org/10.1002/cite.202000195.
[46] Bieber M, Al-Khatib M, Fröde F, Pitsch H, Reddemann MA, Schmid H-J, Tischendorf R, Kneer R. Influence of angled dispersion gas on coaxial atomization, spray and flame formation in the context of spray-flame synthesis of nanoparticles. Exp Fluids 2021;62. https://doi.org/10.1007/s00348-021-03196-6.
[47] Kumar A, Kirchmann J, Beyrau F, Kronenburg A. Jet flapping and its effect on flame oscillations in the SPP1980 SpraySyn burner. Exp Therm Fluid Sci 2023;142:110826. https://doi.org/10.1016/j.expthermflusci.2022.110826.
[48] Stodt MFB, Kiefer J, Fritsching U. Drop dynamics in heterogeneous spray flames for nanoparticle synthesis. Atomiz Spr 2020;30:779–97. https://doi.org/10.1615/AtomizSpr.2020034819.
[49] Beaucage G. Approximations Leading to a Unified Exponential/Power-Law Approach to Small-Angle Scattering. J Appl Crystallogr 1995;28:717–28. https://doi.org/10.1107/S0021889895005292.
[50] Ilavsky J, Jemian PR. Irena tool suite for modeling and analysis of small-angle scattering. J Appl Crystallogr 2009;42:347–53. https://doi.org/10.1107/S0021889809002222.
[51] Günther Porod. Theorie der diffusen Röntgenkleinwinkelstreuung an kolloiden Systemen. Z Naturforsch A 1949;Band 4:401–14. https://doi.org/10.1515/zna-1949-0601.
[52] Bruce DW, O'Hare D, Walton RI. Structure from diffraction methods. Chichester, West Sussex: John Wiley & Sons Ltd; 2014.
[53] No Y, Roe R-J. Methods of X-ray and neutron scattering in polymer science. New York, NY: Oxford Univ. Press; 2000.
[54] Sahouli B, Blacher S, Brouers F, Darmstadt H, Roy C, Kaliaguine S. Surface morphology and chemistry of commercial carbon black and carbon black from vacuum pyrolysis of used tyres. Fuel 1996;75:1244–50. https://doi.org/10.1016/0016-2361(96)00034-8.
[55] Ruland W. Small-angle scattering of two-phase systems: determination and significance of systematic deviations from Porod's law. J Appl Crystallogr 1971;4:70–3. https://doi.org/10.1107/S0021889871006265.
[56] Hyeon-Lee J, Beaucage G, Pratsinis SE, Vemury S. Fractal analysis of flame-synthesized nanostructured silica and titania powders using small-angle X-ray scattering. Langmuir 1998;14:5751–6. https://doi.org/10.1021/la980308s.
[57] Meakin P. Formation of fractal clusters and networks by irreversible diffusion-limited aggregation. Phys Rev Lett 1983;51:1119–22. https://doi.org/10.1103/PhysRevLett.51.1119.
[58] Sorensen CM. Light scattering by fractal aggregates: a review. Aerosol Sci Technol 2001;35:648–87. https://doi.org/10.1080/02786820117868.
[59] Guinier A, Fournet G. Small-angle scattering of X-rays. New York: Wiley; 1955.
[60] Sztucki M, Narayanan T, Beaucage G. In situ study of aggregation of soot particles in an acetylene flame by small-angle x-ray scattering. J Appl Phys 2007;101:114304. https://doi.org/10.1063/1.2740341.
[61] Beaucage G, Kammler HK, Pratsinis SE. Particle size distributions from small-angle scattering using global scattering functions. J Appl Crystallogr 2004;37:523–35. https://doi.org/10.1107/S0021889804008969.